

Azepination-Induced Frontier Molecular Orbital Delocalization of Multiple Resonance Emitters: Constructing Highly Efficient Narrowband Electroluminescent Materials

Tingting Huang,^a Yincai Xu,^{*a} Yupei Qu,^a Xueying Lu,^a Kaiqi Ye,^a and Yue Wang^{*a,b}

^a T. Huang, Dr. Y. Xu, Y. Qu, X. Lu, Prof. K. Ye and Prof. Y. Wang
State Key Laboratory of Supramolecular Structure and Materials
College of Chemistry, Jilin University, Changchun 130012, P. R. China.
E-mails: ycxu17@mails.jlu.edu.cn; yuewang@jlu.edu.cn

^b Prof. Y. Wang
Jihua Laboratory, 28 Huandao Nan Road, Foshan 528200, Guangdong Province, P. R. China.

Keywords: azepine, multiple resonance, thermally activated delayed fluorescence, organic light-emitting diodes, narrowband emission

Abstract: Developing diversified construction strategies for high-color-purity and efficient multiple resonance thermally activated delayed fluorescence (MR-TADF) materials is a major strategic demand to meet the requirements of ultra-high-definition organic light-emitting diode (OLED) displays, posing a significant challenge to the design and synthesis of emitters at the molecular level. Herein, we propose a strategy for azepination-induced frontier molecular orbital (FMO) delocalization of MR emitters, that is, embedding azepine into the prototype molecule BNCz can effectively improve the π -conjugation degree and extend the FMO delocalization, thereby constructing a series of long-wavelength MR-TADF materials with narrowband emission. Through an intramolecular Scholl reaction, these target molecules with an azepine-embedded core are afforded by one-fold heptagonal cyclization of BNCz core and the phenyl ring attached to (aromatic amine-substituted) aryl precursor. They all exhibit efficient green emission around 520 nm and narrow full-widths at half-maximum (FWHMs) of ≤ 38 nm in toluene. OLEDs employing these emitters show excellent electroluminescence (EL) performances, among which *m*-PAZ-BNCz-based OLED exhibits the optimal EL performances with a peak of 528 nm, a FWHM of 37 nm, Commission Internationale de L'Eclairage (CIE) coordinates of (0.26, 0.70), and a maximum external quantum efficiency (EQE) of 36.2%.

1. Introduction

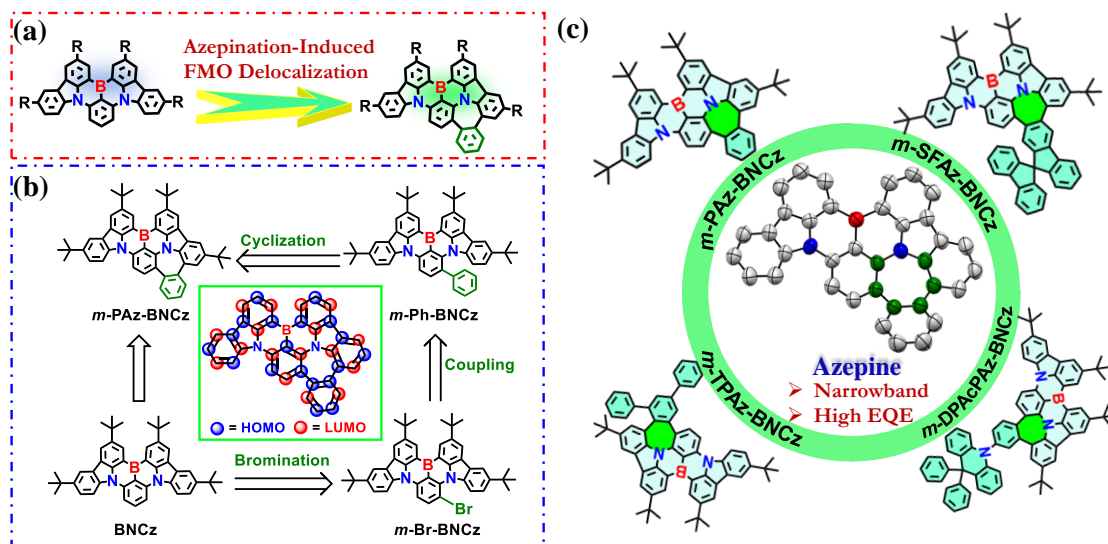
With the rapid growth of downstream consumer electronics application demand and the increasing preference for resource-economical and environmentally friendly displays, the penetration rate and market size of ultra-high-definition (UHD) organic light-emitting diodes (OLED) display products continue to increase.^[1] At present, to meet the major strategic demands of organic electroluminescent displays for high-efficiency and high-color-purity organic luminescent materials, it is paramount to develop monochromatic red, green, and blue luminescent materials with narrow full-width at half-maximum (FWHM),^[2] posing a significant challenge to the design and synthesis of emitters at the molecular level. Encouragingly, the advent of B,N-containing multiple resonance thermally activated delayed fluorescence (MR-TADF) materials with rigid skeletons shows great prospects for UHD displays.^[3] The highest occupied molecular orbital (HOMO) and lowest unoccupied molecular orbital (LUMO) of MR-TADF molecules are alternately distributed on atoms of the rigid skeletons, forming MR transitions with short-range charge transfer (SRCT) states,^[4] coupled with bonding/antibonding characteristics, which suppress high-frequency vibrational coupling and relaxation, and ultimately generate high-efficiency and high-color-purity TADF, fundamentally solving the problem of narrowband emission.^[5]

Early research on MR-TADF materials focused on blue-light-emitting analogs/derivatives derived from DABNA skeleton, while the exploration of long-wavelength emitting materials lagged behind, hindering the progress of panchromatic image displays.^[6] Later, with the birth of sky-blue-light-emitting star MR emitter BNCz ($\lambda_{\text{PL}} = 481 \text{ nm}$, FWHM = 22 nm),^[7] it bears a highly tunable chemical structure and has become an important carrier for the development of long-wavelength MR-TADF materials. For example, by implementing aza-fusion, peripheral decoration, multi-locking, indolo[3,2,1-*jk*]carbazole fusion, polycyclization, and B- π -B and N- π -N arrangement on BNCz framework, different magnitudes of spectral red-shifts are achieved, and narrow FWHMs are maintained.^[8] In addition, it is highlighted that our group

has leveraged frontier molecular orbital engineering (FMOE) strategy to construct charge-transfer excited states and design a series of long-wavelength MR-TADF materials with narrowband emission.^[9] This strategy integrates the advantages of MR skeleton and traditional donor–acceptor (D–A) structure, which is conducive to a wide range of spectral manipulation. Importantly, we have developed two key intermediates for post-functionalization of BNCz via sister reactions of BNCz: Miyaura borylation and bromination, providing the corresponding building blocks (BNCz-Bpin and *m*-Br-BNCz) for subsequent chemical modifications.^[10] Currently, the subsequent derivatization of BNCz with intermediate BNCz-Bpin is developing rapidly,^[11] while the counterpart with intermediate *m*-Br-BNCz is lagging far behind.^[12] When using *m*-Br-BNCz as the substrate, to weaken ICT intensity and narrow FWHM, a phenyl bridge was inserted between donor group and BNCz when we introduced donor group.^[10b] This insertion blocked the direct connection between donor and BNCz, effectively reducing ICT intensity and achieving desired narrowband emission. However, this also resulted in limited spectral red-shift ($\lambda_{\text{PL}} \approx 490$ nm), with the maximum emission being significantly distant from the green primary color ($\lambda_{\text{PL}} = 520\text{--}530$ nm). To satisfy practical application requirements, one should focus not only on FWHM but also on the spectral peak. Assuming that the peak position is far from the primary color window, even a very narrow FWHM may lack practical significance. Therefore, how to further vigorously develop new strategies based on the post-functionalization of intermediate *m*-Br-BNCz to solve the aforementioned issues and achieve a large red-shift in spectrum while maintaining a narrow FWHM poses a huge challenge to molecular design and synthesis. This is also extremely important for subsequent photophysical property investigation, excited-state manipulation, MR molecular library expansion, and material performance research.

In this context, we propose a strategy for azepination-induced frontier molecular orbital (FMO) delocalization of MR emitters, that is, embedding azepine into the prototype molecule BNCz can effectively improve the π -conjugation degree and extend the FMO delocalization

(Scheme 1). This can avoid the unpredictable spectral regulation problem caused by the direct connection of strong/weak push–pull electron groups, and provide an effective molecular paradigm for achieving desired long-wavelength MR-TADF materials with narrowband emission. Herein, the intermediate *m*-Br-BNCz was directly phenyl-substituted via Suzuki cross-coupling to obtain precursor *m*-Ph-BNCz, which was then formed into azepine-embedded *m*-PAz-BNCz by one-fold heptagonal cyclization of precursor *m*-Ph-BNCz via intramolecular Scholl reaction, thereby bonding two carbon atoms with HOMO populations on BNCz moiety and the attached phenyl ring through azepine, effectively inducing enhanced π -conjugation and extended FMO delocalization. Compound *m*-PAz-BNCz exhibits brilliant green emission in toluene with a peak of 519 nm and a FWHM of 38 nm. Compared with the uncyclized precursor *m*-Ph-BNCz ($\lambda_{\text{PL}} = 489$ nm, FWHM = 25 nm), the spectrum undergoes a significant red-shift of 30 nm, and the FWHM does not increase significantly. To investigate the effect of peripheral substituents on the photophysical properties of *m*-PAz-BNCz, representative bulky steric hindrance groups spirobi[fluorene], triphenyl-acridine and triphenyl were introduced to construct *m*-SFAz-BNCz, *m*-DPAcPAz-BNCz and *m*-TPAz-BNCz, respectively. These compounds all demonstrate narrowband vivid green emission. As a result, *m*-PAz-BNCz-based OLED exhibits the optimal electroluminescence (EL) performances, with Commission Internationale de L’Eclairage (CIE) coordinates of (0.26, 0.70) and a maximum external quantum efficiency (EQE) of 36.2%. In fact, *m*-PAz-BNCz can serve as a proof-of-concept model molecule, and there are four unsubstituted sites on the peripheral benzene ring that encapsulates azepine, which can be further modified by donors, acceptors, or moieties without obvious push–pull electron properties through the programmed synthetic roadmap, providing a well-defined template for the construction of various MR-TADF molecules.



Scheme 1. a) Molecular structure diagram of azeption-induced FMO delocalization of MR emitters. b) Retrosynthesis analysis of molecule *m*-PAz-BNCz, with HOMO and LUMO populations diagram of molecule *m*-PAz-BNCz in the box. c) Molecular structures of the investigated compounds, with single crystal structure of *m*-PAz-BNCz in the circle. (ORTEP drawing of the top view is set at 50% probability level, with *t*-Bu groups and hydrogen atoms omitted for clarity.)

2. Results and Discussion

The synthetic protocol of four compounds follows the identical modular synthetic trilogy: bromination, Suzuki coupling and Scholl oxidative coupling (**Figure 1** and Scheme S1). First, BNCz, a well-known microstructural building block, could be easily brominated with *N*-Bromosuccinimide (NBS), and the monobrominated product *m*-Br-BNCz with a well-defined structure, could be successfully isolated. Second, *m*-Br-BNCz was subjected to palladium-mediated Suzuki cross-coupling reaction with various (aromatic amine-substituted) arylboronic acids to give the pivotal pre-cyclized precursors. Finally, in the presence of the oxidant 2,3-dichloro-5,6-dicyano-1,4-benzoquinone (DDQ) and the catalyst Brønsted acid methanesulfonic acid (MSA), intramolecular Scholl oxidation induced direct "stitching" of the carbon atom on the phenyl ring attached to BNCz moiety and the carbon atom on the shoulder of carbazole in BNCz moiety, generating azepine-embedded target compounds. This step is crucial to tether the rotatable attached phenyl ring to MR core BNCz and enable rapid expansion of π -conjugated

system. Efficient intramolecular cyclization derives from two factors: 1) The two carbon atoms desired to be connected have close proximity, so the corresponding chemical reaction is allowed by chemical kinetics. 2) The attached phenyl ring serves as an electron-rich group, and the carbon atom on the shoulder of carbazole in BNCz moiety has HOMO distribution and denser electron cloud density, which is beneficial to intramolecular cyclization (Figure S1). It should be noted that for molecule *m*-SF-BNCz, since there are two potential reaction sites on the substituent 9,9'-spirobi[fluorene], the final cyclization may produce one possible isomer other than *m*-SFAz-BNCz, which is thermodynamically supported (Figure S2a). However, due to the smaller steric hindrance encountered in the generation of molecule *m*-SFAz-BNCz compared to that of isomer, compound *m*-SFAz-BNCz becomes the main product and can be separated with high purity, exceeding 99.0% by high-performance liquid chromatography (HPLC) (Figure S2b). All products were purified by column chromatography and well characterized by NMR and mass spectrometry (Figures S3–S14). The final products were further purified by vacuum gradient sublimation, and single crystal of *m*-PAz-BNCz was cultivated. The HOMO and LUMO energy levels of four molecules estimated by cyclic voltammetry (CV) were -5.13 and -2.64 eV for *m*-PAz-BNCz, -5.11 and -2.91 eV for *m*-SFAz-BNCz, -5.17 and -2.64 eV for *m*-DPAcPAz-BNCz, -5.13 and -2.60 eV for *m*-TPAz-BNCz, respectively (Figure S15). Consequently, the HOMO–LUMO energy level gaps (E_{gap} s) are 2.49, 2.20, 2.53 and 2.53 eV for *m*-PAz-BNCz, *m*-SFAz-BNCz, *m*-DPAcPAz-BNCz and *m*-TPAz-BNCz, respectively. Compared with BNCz (HOMO: -5.40 eV, LUMO: -2.61 eV, E_{gap} : 2.79 eV), the HOMO energy levels of these four molecules rises more and the LUMO energy levels change less, resulting in a decrease in E_{gap} s, which theoretically leads to effective red-shifted emission. The above phenomena are mainly attributed to the introduction of azepine core, which expands the π -conjugation and FMO delocalization. Thermogravimetric analysis (TGA) shows that these compounds all have high thermal stability, and the decomposition and/or sublimation temperatures ($T_{\text{d/s}}$, corresponding to 5% weight loss) of *m*-PAz-BNCz, *m*-SFAz-BNCz, *m*-

DPAcPAZ-BNCz and *m*-TPAZ-BNCz are 432, 487, 480 and 456 °C, respectively (Figure S16), which is conducive to the fabrication of OLED devices by vacuum thermal deposition process.

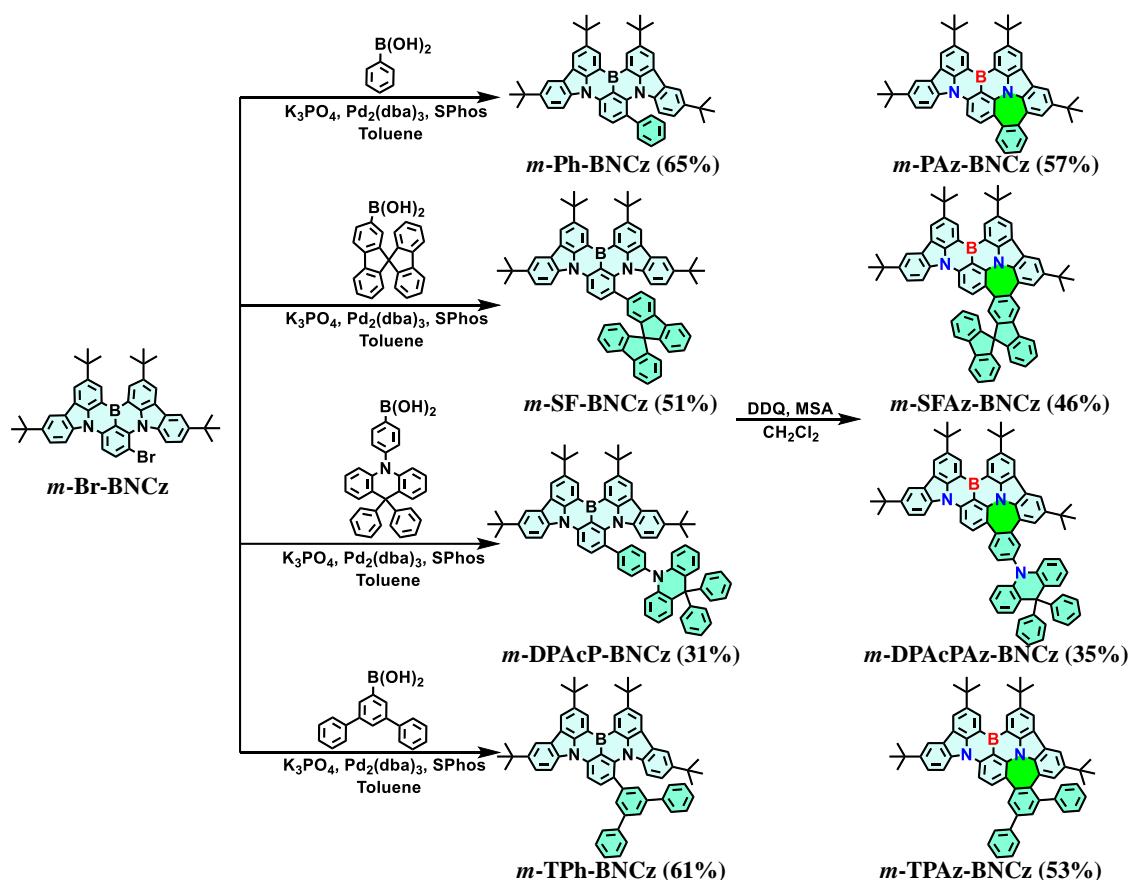


Figure 1. Synthetic procedures of *m*-PAZ-BNCz, *m*-SFAZ-BNCz, *m*-DPAcPAZ-BNCz and *m*-TPAZ-BNCz.

The molecular structure of *m*-PAZ-BNCz was unequivocally confirmed through single-crystal X-ray crystallographic analysis (Figure 2, Figure S17 and Table S1). From the top view, the overall appearance of the molecular skeleton is folded, and the tailing benzene ring is warped, which is caused by the non-planar configuration of the seven-membered ring, making the molecule coupling rigidity and flexibility. The seven-membered ring of azepine in the crystal structure can be divided into seven triangles at its geometric center (centroid), at which the sum of the interior angles of these triangles $s(v)$ is 367.25° . Therefore, the curvature of azepine is $k(v) = 360^\circ - s(v) = -7.25^\circ$, which is a negatively curved carbon.^[13] Viewed from the side, azepine appears folded with an angle of 143.10° . From the side view, the whole molecule appears in a saddle shape, with a saddle length of 9.429 \AA and a depth of 0.926 \AA . In

the three-dimensional stacking structure of crystal, *m*-PAz-BNCz does not have any special shaped arrangement patterns, and no perceptible $\pi\cdots\pi$ stacking interactions are observed between any adjacent molecules. Intriguingly, in each unit cell of the crystals, (*P*)- and (*M*)-enantiomers coexist in equal equivalents. However, due to the lack of significant steric hindrance from the chiral hetero[4]helicene and the absence of strong symmetry-breaking factors in the helical skeleton, the energy barrier of racemization for such chiral [4]helicene at room temperature is typically low.^[14] This low energy barrier of racemization has hindered further investigations into chiral-related resolution and properties.

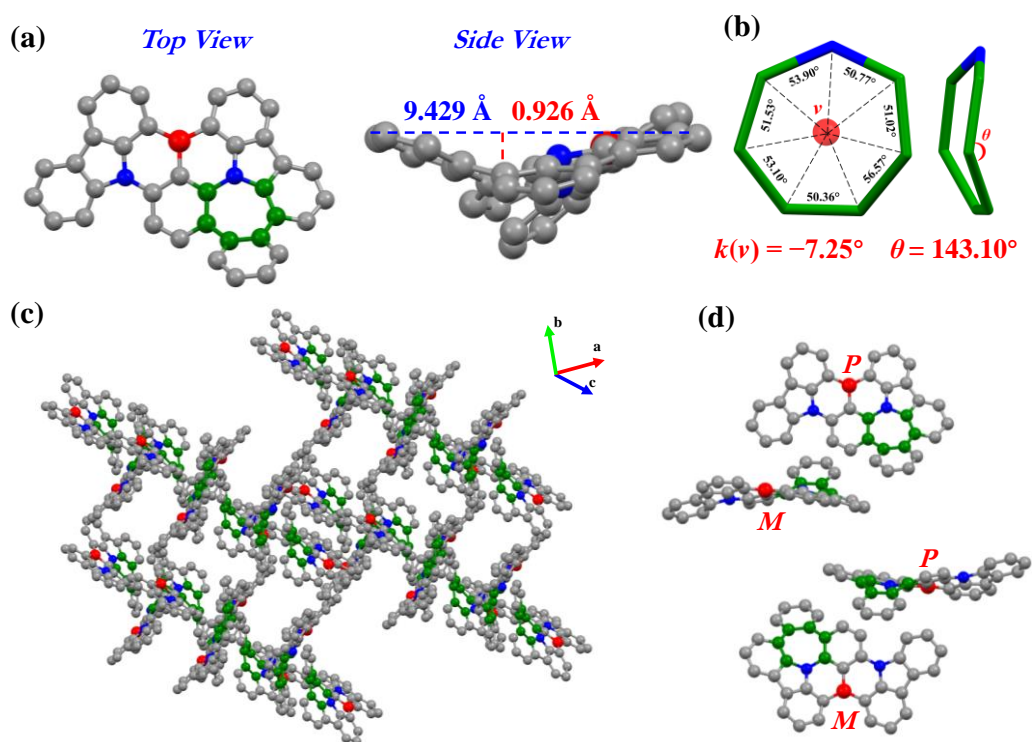


Figure 2. Single crystal structure analysis of *m*-PAz-BNCz. Ball and Stick drawings of the top and side views are set, with *t*-Bu groups and hydrogen atoms omitted for clarity. a) Crystal structure. b) Gaussian curvature. c) Stacking modes. d) (*P*/*M*)-enantiomers.

To comprehensively understand the effects and differences of azepine-embedding on geometric structure and electronic properties, density functional theory (DFT) and time-dependent DFT (TDDFT) calculations were performed for these four investigated molecules with different push–pull electron characteristics. The HOMO and LUMO distributions, E_{gap} s, and oscillator strengths (f_s) of *m*-PAz-BNCz, *m*-SFAz-BNCz, *m*-DPAcPAz-BNCz and *m*-

TPAz-BNCz were analyzed and compared (**Figure 3**). All these four molecules exhibit similar LUMO distributions, roughly analogous to BNCz core, predominantly localized on the boron atom and *ortho/para*-positions of the carbon atoms connected to the boron atom. Their HOMOs are slightly different, primarily distributed on the nitrogen atoms and *ortho/para*-positions of the carbon atoms connected to the nitrogen atoms within BNCz core, and partially extending to the peripheral benzene ring that encapsulates azepine. As a result, the E_{gap} s of these molecules are distinctly reduced compared with that of BNCz (E_{gap} : 3.35 eV), potentially promoting red-shifts in their emission spectra. The π -conjugation degrees of these four molecules are significantly enhanced due to the embedding of azepine core, which is highly consistent with our proposed strategy for azepination-induced FMO delocalization of MR emitters. Taking the proof-of-concept model molecule *m*-PAz-BNCz as an example, it has a more dispersed FMO distribution compared with its corresponding uncyclized precursor *m*-Ph-BNCz, so relatively strong long-range charge transfer (LRCT) will occur during the Franck–Condon vertical absorption transition process. Therefore, the E_{gap} of *m*-PAz-BNCz (3.16 eV) decreases compared with that of *m*-Ph-BNCz (3.25 eV) (Figure S1), suggesting that *m*-PAz-BNCz may undergo bathochromic shift. The oscillator strengths of these four molecules are relatively large, indicating that the probability of electronic transition in molecule is high after absorbing incident photons, which is more conducive to facilitating high photoluminescence quantum yields (Φ_{PLS}) for MR emitters with intrinsically strong rigid skeletons.

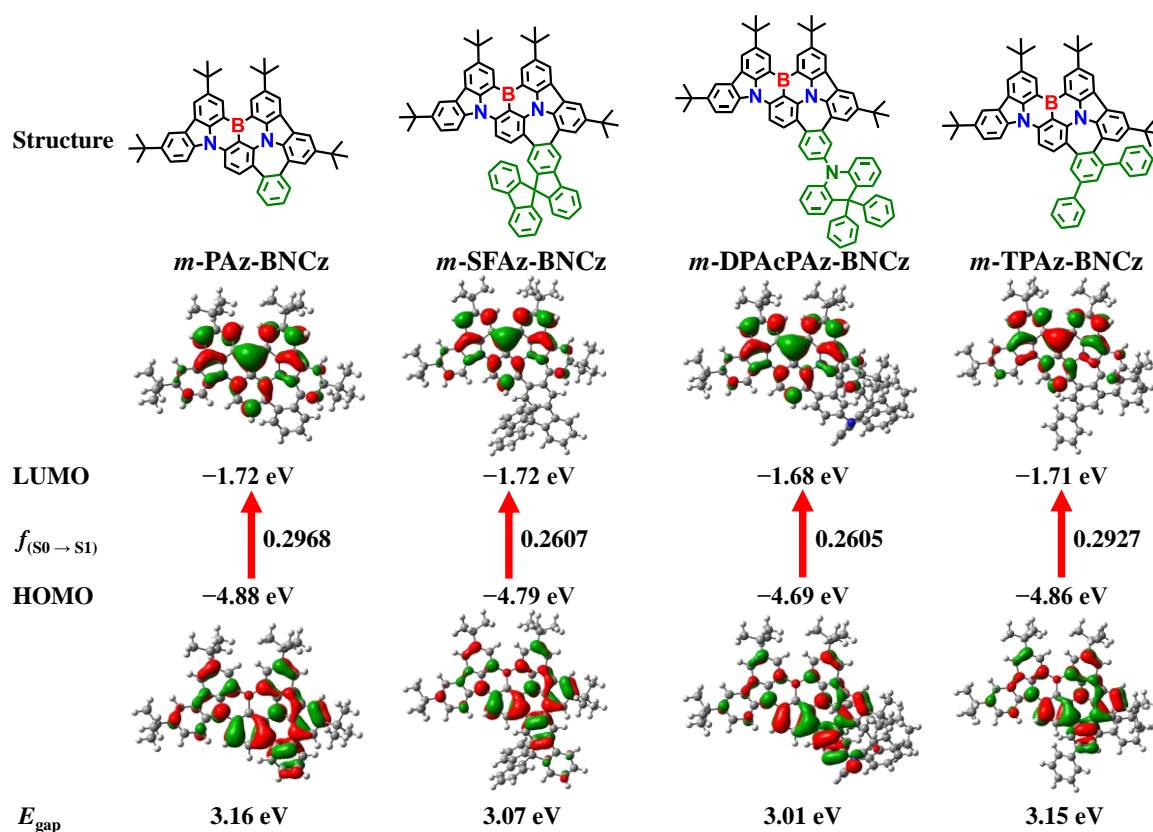


Figure 3. HOMO/LUMO distributions, HOMO–LUMO energy level gaps (E_{gaps}), oscillator strengths (f_s) of the investigated molecules.

The fundamental photophysical properties of *m*-PAz-BNCz, *m*-SFAz-BNCz, *m*-DPAcPAz-BNCz and *m*-TPAz-BNCz were conducted in toluene solution (1×10^{-5} M, **Figure 4** and **Table 1**). The ultraviolet–visible (UV–vis) absorption and photoluminescence (PL) spectral profiles of these four molecules all exhibit good mirror symmetry, with intense absorption and emission peaks of 493 and 519 nm for *m*-PAz-BNCz, 497 and 523 nm for *m*-SFAz-BNCz, 491 and 515 nm for *m*-DPAcPAz-BNCz, and 494 and 521 nm for *m*-TPAz-BNCz, respectively. Accordingly, these four molecules show small Stokes shifts of 26, 26, 24 and 27 nm, and maintain narrow FWHMs of 38, 37, 34 and 38 nm, respectively. As a result, the CIE coordinates of *m*-PAz-BNCz, *m*-SFAz-BNCz, *m*-DPAcPAz-BNCz and *m*-TPAz-BNCz correspond to (0.26, 0.64), (0.26, 0.67), (0.21, 0.66) and (0.25, 0.66), respectively, which are very close to the standard green light CIE coordinates of (0.21, 0.71) stipulated by the National Television Standards Committee (NTSC).^[15] The above results are consistent with the predictions of theoretical

calculations, and the overall spectral properties of molecules *m*-SFAz-BNCz, *m*-DPAcPAz-BNCz and *m*-TPAz-BNCz do not change much relative to that of *m*-PAz-BNCz. Taking *m*-PAz-BNCz as an intuitive example, the formation of azepine core enhances the π -conjugation of the entire molecular framework, which makes the absorption and emission of *m*-PAz-BNCz red-shifted by 19 and 30 nm compared with its sky-blue-light-emitting precursor *m*-Ph-BNCz ($\lambda_{\text{abs}} = 474$ nm, $\lambda_{\text{PL}} = 489$ nm) (Figure S18), demonstrating the effectiveness of azepination-induced FMO delocalization. Compounds *m*-PAz-BNCz, *m*-SFAz-BNCz, *m*-DPAcPAz-BNCz and *m*-TPAz-BNCz in oxygen-free toluene solution all exhibit high Φ_{PLS} of 98%, 93%, 98% and 94%, respectively. Moreover, according to the onset values of fluorescence and phosphorescence spectra measured at 77 K (Figure S19), singlet–triplet energy splittings (ΔE_{STS}) were estimated to be 0.13, 0.15, 0.13 and 0.11 eV for *m*-PAz-BNCz, *m*-SFAz-BNCz, *m*-DPAcPAz-BNCz and *m*-TPAz-BNCz, respectively. These small ΔE_{ST} values are adequate to support the upconversion of excitons from the lowest triplet (T_1) state to the lowest singlet (S_1) state, promoting the generation of TADF properties. All characteristic photophysical properties can be attributed to their highly rigid MR skeletons, resulting in less structural deformation during the transition of molecules from the ground (S_0) state to S_1 state.

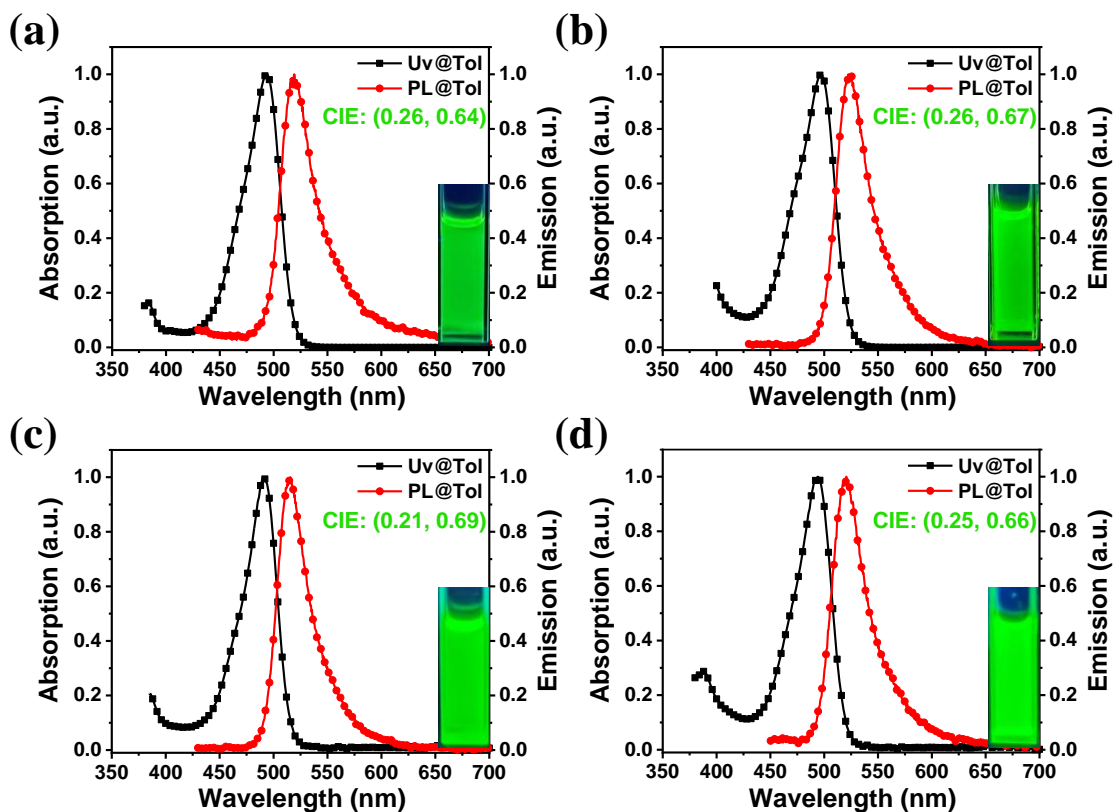


Figure 4. Normalized UV–vis absorption and fluorescence spectra of compounds *m*-PAZ-BNCz (a), *m*-SFAZ-BNCz (b), *m*-DPAcPAZ-BNCz (c) and *m*-TPAZ-BNCz (d) measured in toluene solution. (1×10^{-5} M, 298 K; Inset: photograph in toluene taken under 365 nm UV light.)

Table 1. Summary of photophysical properties of compounds.

compound	$\lambda_{\text{abs}}^{\text{a}}$ [nm]	$\lambda_{\text{em}}^{\text{b}}$ [nm]	FWHM ^c [nm]	$E_{\text{S}_1}^{\text{d}}$ [eV]	$E_{\text{T}_1}^{\text{e}}$ [eV]	$\Delta E_{\text{ST}}^{\text{f}}$ [eV]	E_{g}^{g} [eV]	HOMO ^h [eV]	LUMO ^h [eV]	$\Phi_{\text{PL}}^{\text{i}}$ [%]
<i>m</i> -PAZ-BNCz	493	519	38	2.52	2.39	0.13	2.46	-5.13	-2.64	98
<i>m</i> -SFAZ-BNCz	497	523	37	2.50	2.35	0.15	2.36	-5.11	-2.91	93
<i>m</i> -DPAcPAZ-BNCz	491	515	34	2.52	2.39	0.13	2.40	-5.17	-2.64	98
<i>m</i> -TPAZ-BNCz	494	521	38	2.51	2.39	0.11	2.34	-5.13	-2.60	94

^a) Peak wavelength of the lowest energy absorption band. ^b) Peak wavelength of the PL spectrum in toluene solution (1×10^{-5} M, 298 K). ^c) Full-width at half-maximum. ^d) Singlet energy estimated from the onset of the fluorescence spectrum in toluene solution (1×10^{-5} M, 77 K). ^e) Triplet energy estimated from the onset of the phosphorescence spectrum in a frozen toluene matrix (1×10^{-5} M, 77 K). ^f) $\Delta E_{\text{ST}} = E_{\text{S}_1} - E_{\text{T}_1}$. ^g) Optical band gap estimated from the absorption edge of the UV–vis spectrum. ^h) Determined from cyclic voltammetry using the formula: $E_{\text{HOMO}} = -(E_{\text{ox}} + 4.8)$ eV and $E_{\text{LUMO}} = -(E_{\text{red}} + 4.8)$ eV. ⁱ) Absolute photoluminescence quantum yield measured with an integrating sphere in N₂-bubbling toluene solution (1×10^{-5} M, 298 K).

Given that the four compounds exhibit similar spectral properties and that *m*-SFAZ-BNCz, *m*-DPAcPAZ-BNCz and *m*-TPAZ-BNCz could be considered as peripheral chemical modifications of *m*-PAZ-BNCz, *m*-PAZ-BNCz was selected as a representative model molecule

for subsequent in-depth theoretical calculation discussions to understand the structure-property relationship. The calculated root-mean-square deviation (RMSD) of *m*-PAz-BNCz is 0.0773 Å (Figure S20), and the reorganization energy is 0.23 eV (Figure S21).^[16] These values are relatively small, which can quantitatively demonstrate that there is only a small structural deformation of the overall molecular structure during the electronic excitation process from S₀ state to S₁ state, and also support its small Stokes shift and narrow FWHM. Subsequently, the Huang–Rhys factor was calculated from the reorganization energy decomposition to visually quantify the relationship between structural fluctuations and molecular vibrational modes of molecule *m*-PAz-BNCz during the transition from S₀ state to S₁ state (Figure S22). Generally, enhancing low-frequency and suppressing high-frequency vibronic coupling are conducive to narrowing FWHM, that is, the greater the contribution of low-frequency region to the Huang–Rhys factor, the easier it is to achieve narrowband emission.^[17] The dominant Huang–Rhys factors for S₁ → S₀ (> 0.20) in *m*-PAz-BNCz mainly consist of low-frequency region with scissoring, twisting, in-plane, and out-of-plane rocking vibrational modes.^[18] The corresponding representative normal vibration modes that contribute more to reorganization energies are all located in the low-frequency region (< 180 cm⁻¹). Especially, in the two relatively high-frequency regions (71.18 and 167.45 cm⁻¹), which are mainly characterized by the in-plane and out-of-plane rocking of the peripheral benzene ring that encapsulates azepine in the luminophore, which is also the principal reason for broadening the FWHM compared with that of BNCz.

To analyze and understand the impact of the incorporation of azepine on excited states, hole–electron analysis was performed on the uncyclized precursor *m*-Ph-BNCz and the cyclized molecule *m*-PAz-BNCz.^[19] To facilitate the discussion of the relevant properties of holes and electrons, the molecular structures of *m*-Ph-BNCz and *m*-PAz-BNCz were divided into two fragments: the phenyl (Ph) group attached to the *meta*-position of B-substituted phenyl ring, and BNCz core. It can be intuitively observed from the hole–electron distribution plot that the

holes and electrons of *m*-Ph-BNCz and *m*-PAz-BNCz are well separated (Figure S23), with the majority concentrated on fragment BNCz, while a small fraction of holes was extended to fragment Ph. In addition, after the incorporation of azepine, the hole distribution on fragment Ph increases significantly. In view of this, heat maps of *m*-Ph-BNCz and *m*-PAz-BNCz were plotted and compared to more clearly quantify the contribution of each fragment to hole and electron generation (Figure S24). For *m*-Ph-BNCz and *m*-PAz-BNCz, most of the holes and electrons are primarily concentrated on fragment BNCz. After the embedding of azepine, the hole proportion on fragment Ph (11.06%) of *m*-PAz-BNCz increases significantly, almost two-fold that of *m*-Ph-BNCz (5.87%), which may induce a significant enhancement of LRCT intensity. Moreover, the interfragment charge transfer (IFCT) of *m*-Ph-BNCz and *m*-PAz-BNCz was calculated and compared to quantitatively assess the specific electron transfer behavior during the electronic excitation process.^[20] Based on the intrafragment electron redistribution of fragment (IFER) (Table S2), the electron redistribution of *m*-Ph-BNCz and *m*-PAz-BNCz during the electronic excitation process mainly occurs inside fragment BNCz, but with slight differences. The IFER value of fragment BNCz in *m*-PAz-BNCz (0.88703) is decently compared with that of *m*-Ph-BNCz (0.93811). This indicates that both molecules are dominated by SRCT occurring within fragment BNCz, but the embedding of azepine leads to the expansion of hole delocalization, which is consistent with the enhanced FMO delocalization, resulting in an increase in the LRCT proportion. This conclusion can also be accurately confirmed from the net electron transfer from fragment Ph to fragment BNCz and the specific percentage of SRCT/LRCT in molecules *m*-Ph-BNCz and *m*-PAz-BNCz (Tables S3–S4). The net electron transfer amount in azepine-embedded *m*-PAz-BNCz (0.10798) is nearly twice that of uncyclized precursor *m*-Ph-BNCz (0.05537), and the percentage of LRCT *m*-PAz-BNCz (11.27%) increases significantly, almost twice that of *m*-Ph-BNCz (6.17%). This increase is the key factor promoting the remarkably red-shifted emission of *m*-PAz-BNCz.

To further understand the photophysical properties of these four compounds in blended films, they were doped as emitters into host matrix 9-(3-(6-phenyl-9*H*-pyrido[2,3-*b*]indol-9-yl)phenyl)-9*H*-3,9'-bicarbazole (PhCbBCz) with 3 wt% doping concentration to fabricate thin films.^[21] All doped films exhibit efficient green emission (Figure S25 and Table S5), and display slight red-shifts and broadened FWHMs compared with their emission in toluene, which is attributed to the intricate molecular interactions between host and emitter, between emitter and emitter, and the ambipolar effect of PhCbBCz. Under room temperature and vacuum atmosphere, the transient PL decay curves of these doped films exhibit bi-exponential decay appearance (Figure S26 and Table S6), comprising of nanosecond-scale prompt fluorescence and microsecond-scale delayed fluorescence. As the temperature rises from 80 K to 320 K, the proportion of delayed fluorescence component gradually increases (Figure S27). These typical features unequivocally verify the TADF characteristics of these four emitters. By fitting the transient PL decay curves, the actual lifetime and corresponding ratio of prompt fluorescence and delayed fluorescence can be obtained; combined with Φ_{PL} values, various photophysical rate constants can be acquired. The results show that the rate constant of prompt fluorescence (k_{F}) of all compounds is greater than the rate constant of internal conversion (k_{IC}), indicating that their non-radiative decay energy losses are minimized, which is consistent with their high Φ_{PLS} (97 %, 90%, 95% and 92% for *m*-PAZ-BNCz, *m*-SFAZ-BNCz, *m*-DPAcPAZ-BNCz and *m*-TPAZ-BNCz, respectively) (Table S6). These excellent photophysical properties indicate their potential to achieve excellent EL performances.

The EL performances of these four compounds as emitters were evaluated by vacuum-deposited OLEDs with the configuration of [ITO/TAPC (50 nm)/TCTA (5 nm)/PhCbBCz: *x* wt% the investigated compounds (*x* = 3, 5, 10, and 20) (30 nm)/TmPyPB (30 nm)/LiF (1 nm)/Al (100 nm)] (Figure S28). ITO (indium tin oxide) and Al (aluminum) were used as anode and cathode, respectively. TAPC (1,1-bis[(di-4-tolylamino)phenyl]cyclohexane), TCTA (tris(4-carbazolyl-9-ylphenyl)amine), and TmPyPB (3,3'-[5'-[3-(3-pyridinyl)phenyl]][1,1':3',1''-

terphenyl]-3,3"-diyl]bispyridine) were designated as the hole transporting layer (HTL), electron blocking layer (EBL), and electron transporting layer (ETL), respectively, which can promote the efficient injection and transport of carriers while restricting excitons within the emitting layer (EML), thereby ensuring efficient energy transfer. The wide band gap, high triplet energy ($E_{T1} = 2.93$ eV) and well-balanced ambipolar charge carrier transport capability of PhCbBCz are beneficial for confining the exciton recombination region, inhibiting energy back transfer, and reduce energy loss. Therefore, PhCbBCz was selected as the host of EML. In addition, doping concentrations of 3, 5, 10, and 20 wt% were implemented for these emitters to optimize EL performances of the corresponding devices. The corresponding EL spectra and EQE–luminance (L) curves are shown in **Figure 5**; other device performances and detailed parameters including current density (J), voltage (V), luminance, current efficiency (CE) and power efficiency (PE) are depicted in Figures S29–S30, **Table 2** and Table S7.

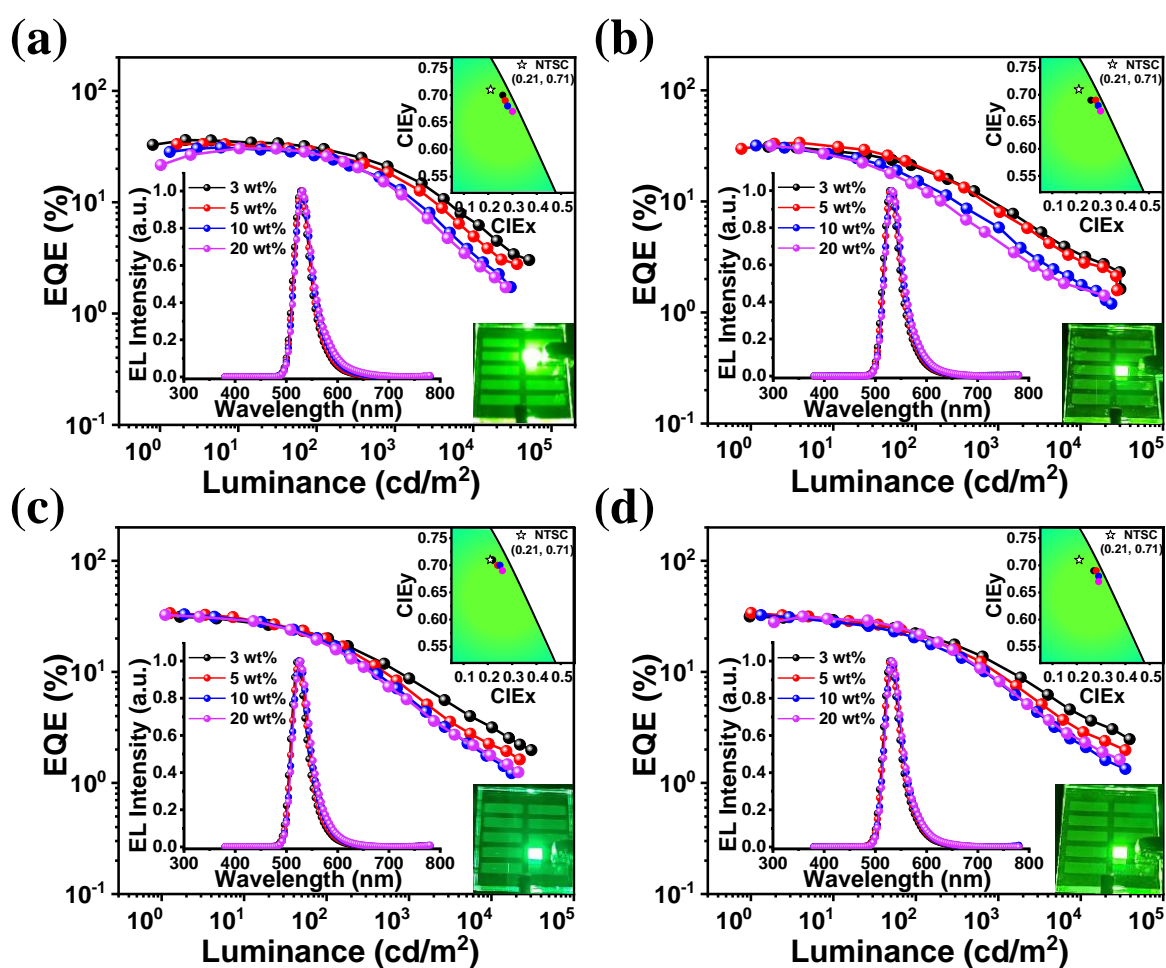


Figure 5. EL spectra (inset) and EQE–*L* curves of the devices with the configuration of [ITO/TAPC (50 nm)/TCTA (5 nm)/PhCbBCz: *x* wt% *m*-PAz-BNCz (a), PhCbBCz: *x* wt% *m*-SFAz-BNCz (b), PhCbBCz: *x* wt% *m*-DPAcPAz-BNCz (c), and PhCbBCz: *x* wt% *m*-TPAz-BNCz (d) (30 nm) (*x* = 3, 5, 10, 20)/TmPyPB (30 nm)/LiF (1 nm)/Al (100 nm)]. (Inset: The color coordinates of the devices on the CIE 1931 color space and photograph showing the emission color of the device at 3 wt% doping concentration.)

Table 2. Summary of EL data of devices (host: PhCbBCz) based on emitters with the optimal doping concentration.

compound (<i>x</i> wt%)	λ_{em}^a [nm]	FWHM ^{b)} [nm]	CIE(<i>x</i> , <i>y</i>) ^{c)}	V_{on}^d [V]	L_{max}^e [cd m ⁻²]	CE_{max}^f [cd A ⁻¹]	PE_{max}^g [lm W ⁻¹]	EQE ^{h)} [%]
<i>m</i> -PAz-BNCz (3)	528	37	(0.26, 0.70)	3.0	51900	132.1	133.9	36.2/30.8/19.5
<i>m</i> -SFAz-BNCz (5)	532	38	(0.28, 0.69)	3.0	27730	129.1	128.1	33.7/21.1/8.2
<i>m</i> -DPAcPAz-BNCz (5)	524	37	(0.24, 0.70)	3.0	22090	129.0	135.1	33.8/19.7/6.8
<i>m</i> -TPAz-BNCz (5)	532	38	(0.28, 0.69)	3.0	34840	125.2	131.1	33.9/21.9/9.6

^{a)} EL peak wavelength. ^{b)} Full-width at half-maximum. ^{c)} Commission Internationale de L'Eclairage coordinates (value taken at 100 cd m⁻²). ^{d)} Turn-on voltage at 1 cd m⁻². ^{e)} Maximum luminance. ^{f)} Maximum current efficiency. ^{g)} Maximum power efficiency. ^{h)} Maximum external quantum efficiency, and values at 100 and 1000 cd m⁻², respectively.

All devices exhibit efficient carrier injection and transport with low turn-on voltages of ≤ 3.1 V (V_{on} at 1 cd m⁻²). The turn-on voltage gradually decreases with the doping concentration increases, indicating that at high doping concentrations, carriers prefer to be directly injected into the emitter rather than transported through PhCbBCz. All emitters can achieve complete energy transfer at 3 wt% doping concentration, and the device based on 3 wt% doping concentration emitter *m*-PAz-BNCz exhibits the optimal EL performances, specifically showing high color purity: a peak of 528 nm, a narrow FWHM of 37 nm, CIE coordinates of (0.26, 0.70), and high efficiency: maximum EQE, CE and PE of 36.2%, 132.1 cd A⁻¹, and 133.9 lm W⁻¹, respectively. In contrast, OLEDs employing *m*-SFAz-BNCz, *m*-DPAcPAz-BNCz and *m*-TPAz-BNCz with bulky steric substituents as emitters exhibit the best EL performances at 5 wt% doping concentration. They display vibrant green emission with peaks, FWHMs and CIE coordinates of 532 nm, 38 nm and (0.28, 0.69) for *m*-SFAz-BNCz; 524 nm, 37 nm and (0.24, 0.70) for *m*-DPAcPAz-BNCz; and 532 nm, 38 nm and (0.28, 0.69) for *m*-TPAz-BNCz, respectively. Meanwhile, they achieve maximum EQE, CE and PE of 33.7%, 129.1 cd A⁻¹, 128.1 lm W⁻¹ for *m*-SFAz-BNCz; maximum EQE, CE and PE of 33.8%, 129.0 cd A⁻¹ and 135.1

cd A⁻¹ for *m*-DPAcPAz-BNCz; and maximum PEs of 33.9%, 125.2 cd A⁻¹ and 131.1 lm W⁻¹ for *m*-TPAz-BNCz, respectively. In addition, within the doping concentration range of 3–20 wt%, the maximum EQEs of these emitters-based devices all exceed 30.0%, especially the maximum EQEs of *m*-SFAz-BNCz-, *m*-DPAcPAz-BNCz- and *m*-TPAz-BNCz-based devices remain basically unchanged, reflecting a small concentration-independence of device performances, which is closely related to the bulky steric hindrance groups on the periphery of their molecular structures, which can enlarge the intermolecular distance in the EML and effectively inhibit the intermolecular stacking quenching. This can be confirmed by the absence of detectable $\pi \cdots \pi$ stacking interactions between adjacent molecules in the three-dimensional stacking structure of *m*-PAz-BNCz crystal. As a result, the single host-based devices based on these four emitters all show high exciton utilization efficiency, with maximum luminance of more than 20000 cd m⁻², especially *m*-PAz-BNCz-based devices, with maximum luminance of more than 50000 cd m⁻². Moreover, the CIE coordinates of these four emitter-based devices vary slightly within the doping concentration range of 3–20 wt%, and the CIE_y values are all maintained above 0.67, which is very close to the standard green light CIE coordinates (0.21, 0.71) specified by NTSC. In fact, this provides a new molecular design paradigm for constructing efficient devices that can counteract the common aggregation-caused quenching effect in devices and is not easily affected by doping concentration, which has important practical significance for improving the controllability and repeatability of devices, simplifying manufacturing processes, and saving production costs. All these well-fabricated devices exhibit robust spectral stability over a wide voltage range of 3–8 V (Figures S31), indicating that there is only one stable fixed exciton recombination region located in the EML within these device architectures.

The device efficiency roll-offs of *m*-SFAz-BNCz-, *m*-DPAcPAz-BNCz- and *m*-TPAz-BNCz-based devices with 3 wt% doping concentration are steeper than that of *m*-PAz-BNCz-based device with 3 wt% doping concentration,^[22] which may be attributed to the fastest rate

constant of reverse intersystem crossing (k_{RISC} , $1.34 \times 10^4 \text{ s}^{-1}$) of the corresponding doped film based on *m*-PAZ-BNCz, mainly due to its shortest lifetime of delayed fluorescence (τ_{TADF} , 70.0 μs), compared with these of the doped films based on *m*-SFAZ-BNCz (k_{RISC} , $0.25 \times 10^4 \text{ s}^{-1}$, τ_{TADF} , 321.3 μs), *m*-DPAcPAZ-BNCz (k_{RISC} , $0.33 \times 10^4 \text{ s}^{-1}$, τ_{TADF} , 272.9 μs) and *m*-TPAZ-BNCz (k_{RISC} , $0.62 \times 10^4 \text{ s}^{-1}$, τ_{TADF} , 136.7 μs). At luminance of 1000 cd m^{-2} , the efficiency roll-off ratios are 46.1%, 70.0%, 71.9% and 63.5% for *m*-PAZ-BNCz-, *m*-SFAZ-BNCz-, *m*-DPAcPAZ-BNCz- and *m*-TPAZ-BNCz-based devices with 3 wt% doping concentration, respectively. Subsequently, to alleviate the efficiency roll-off problem, a direct and effective approach is to introduce a matching sensitizer into the EML.^[23] The classical TADF material DACT-II (9-[4-(4,6-diphenyl-1,3,5-triazin-2-yl)phenyl]-*N,N,N',N''*-tetraphenyl-9*H*-carbazole-3,6-diamine) has ultra-high Φ_{PL} ($\approx 100\%$) and sufficient k_{RISC} ($6.88 \times 10^4 \text{ s}^{-1}$),^[24] which can quickly capture triplet excitons and achieve rapid upconversion and widely selected as a sensitizer to optimize the green-light-emitting device performances. Simultaneously, the decent overlap between its emission spectrum and the absorption spectra of these four investigated emitters is conducive to the efficient energy transfer from sensitizer to emitter (Figure S32). Next, the sensitized OLEDs were fabricated via vacuum thermal deposition with the configuration similar to that of the single host-based devices, except that sensitizer DACT-II with 25 wt% doping concentration was incorporated into the EML (Figure S33). The EL spectra and EQE-*L* curves are shown in **Figure 6**, the *J-V-L* curves, CE-*L* and PE-*L* curves are displayed in Figures S34–S35, and the comprehensive EL performance parameters are compiled in **Table 3** and Table S8.

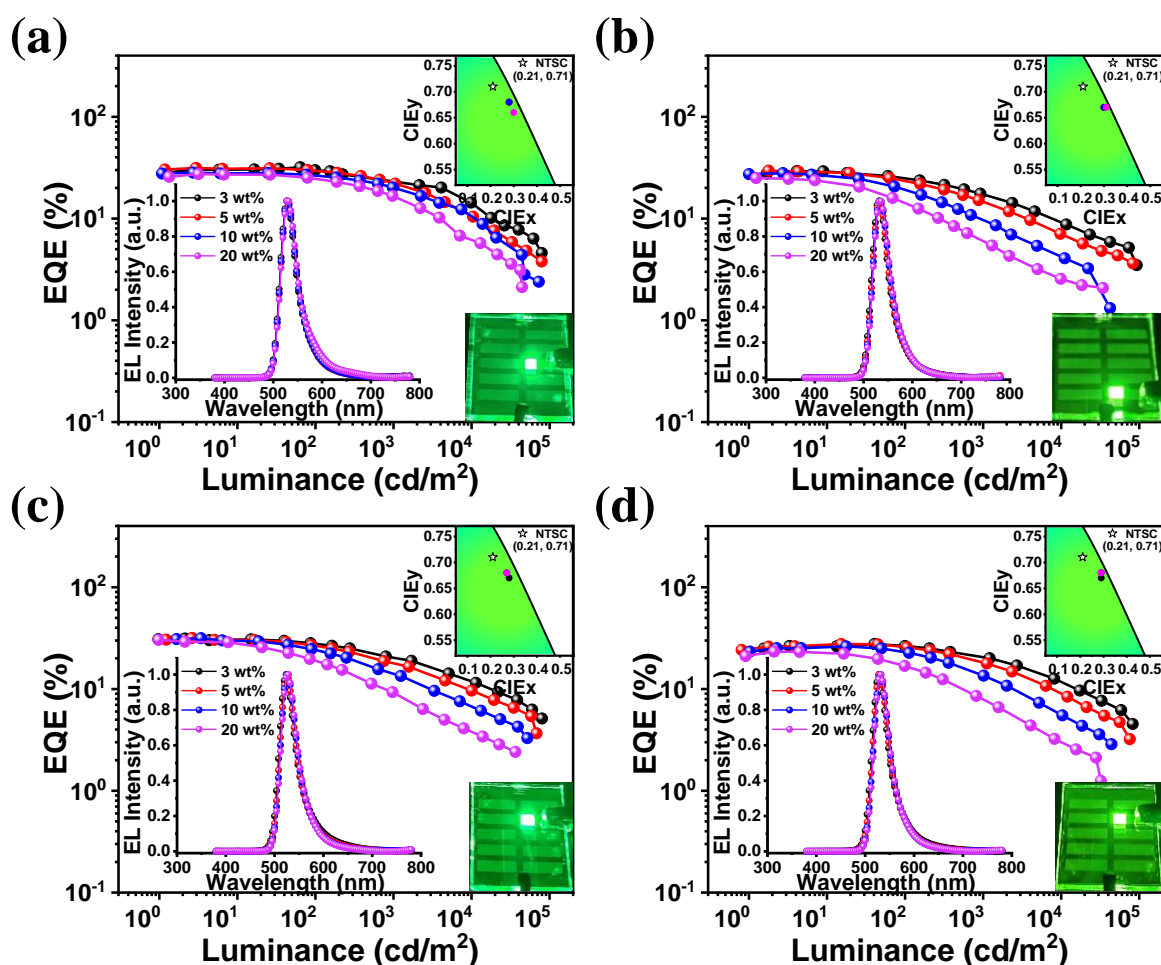


Figure 6. EL spectra (inset) and EQE– L curves of the devices with the configuration of [ITO/TAPC (50 nm)/TCTA (5 nm)/PhCbBCz: 25 wt% DACT-II: x wt% m -PAZ-BNCz (a), PhCbBCz: 25 wt% DACT-II: x wt% m -SFAZ-BNCz (b), PhCbBCz: 25 wt% DACT-II: x wt% m -DPACPAZ-BNCz (c), and PhCbBCz: 25 wt% DACT-II: x wt% m -TPAZ-BNCz (d) (30 nm) ($x = 3, 5, 10, 20$)/TmPyPB (30 nm)/LiF (1 nm)/Al (100 nm)]. (Inset: The color coordinates of the devices on the CIE 1931 color space and photograph showing the emission color of the device at 3 wt% doping concentration.)

Table 3. Summary of EL data of devices (host: PhCbBCz, sensitizer: DACT-II) based on emitters with the optimal doping concentration.

compound (x wt%)	λ_{em}^a [nm]	FWHM ^b [nm]	CIE(x, y) ^c	V_{on}^d [V]	L_{max}^e [cd m ⁻²]	CE _{max} ^f [cd A ⁻¹]	PE _{max} ^g [lm W ⁻¹]	EQE ^h [%]
m -PAZ-BNCz (3)	528	39	(0.28, 0.68)	2.6	79100	118.9	131.5	31.9/30.0/23.1
m -SFAZ-BNCz (5)	532	40	(0.30, 0.67)	2.7	82790	111.9	130.2	29.6/23.4/14.6
m -DPACPAZ-BNCz (5)	524	39	(0.27, 0.68)	2.8	68280	117.3	127.0	31.7/26.6/17.9
m -TPAZ-BNCz (5)	528	39	(0.29, 0.68)	2.8	75600	108.5	111.0	27.7/25.9/18.2

^a) EL peak wavelength. ^b) Full-width at half-maximum. ^c) Commission Internationale de L'Éclairage coordinates (value taken at 100 cd m⁻²). ^d) Turn-on voltage at 1 cd m⁻². ^e) Maximum luminance. ^f) Maximum current efficiency. ^g) Maximum power efficiency. ^h) Maximum external quantum efficiency, and values at 100 and 1000 cd m⁻², respectively.

The sensitized devices of all doping concentrations exhibit lower turn-on voltages (2.6–2.9 V) compared with that of the single host-based devices of the corresponding doping concentrations, indicating that the introduction of sensitizer DACT-II further promotes carrier injection and transport. The optimal doping concentrations of the sensitized devices based on the investigated emitters are the same as those of the corresponding single host-based devices. They all emit bright green light with peaks of 524–532 nm and maintain narrow FWHMs of around 39 nm. The corresponding CIE coordinates are (0.28, 0.68), (0.30, 0.67), (0.27, 0.68), and (0.29, 0.68) for *m*-PAz-BNCz-, *m*-SFAz-BNCz-, *m*-DPAcPAz-BNCz- and *m*-TPAz-BNCz-based devices, respectively. The maximum EQE, CE and PE are 31.9%, 118.9 cd A⁻¹ and 131.5 lm W⁻¹ for *m*-PAz-BNCz; 29.6%, 111.9 cd A⁻¹ and 130.2 lm W⁻¹ for *m*-SFAz-BNCz; 31.7%, 117.3 cd A⁻¹ and 127.0 lm W⁻¹ for *m*-DPAcPAz-BNCz; and 27.7%, 108.5 cd A⁻¹ and 111.0 lm W⁻¹ for *m*-TPAz-BNCz, respectively. Furthermore, the participation of DACT-II further boosts the maximum luminance of all devices, reaching 79100, 82790, 68280 and 75600 cd m⁻², respectively. The maximum EQEs of the sensitized devices are slightly lower than that of the single host-based devices, which may be due to the dissipation in the energy transfer process from S₁ of sensitizer to that of emitter. In addition, the incorporation of sensitizer DACT-II greatly alleviates the efficiency roll-offs of devices, and the efficiency roll-off ratios (at luminance of 1000 cd m⁻²) are 27.6%, 41.1%, 35.1% and 25.6% for *m*-PAz-BNCz-, *m*-SFAz-BNCz-, *m*-DPAcPAz-BNCz- and *m*-TPAz-BNCz-based devices with 3 wt% doping concentration, respectively, indicating that the involvement of sensitizer DACT-II significantly promotes the upconversion of triplet excitons. For the devices based on specific emitters, the efficiency roll-off of gradually becomes more severe with the doping concentration increases. The most legitimate explanation for this phenomenon is that at high doping concentrations (especially 10 and 20 wt% doping concentration), there may be two competing excited state energy consumption pathways, including the direct charge trapping on emitters and short-range Dexter energy transfer (DET) channel unlocking from T₁ of DACT-II to that of emitter (Figure

S36).^[25] The activation of DET channel charge trapping will result in the accumulation of triplet excitons, accelerate the collision and annihilation of triplet excitons at high luminance, and ultimately lead to energy leakage. Furthermore, all devices maintain excellent spectral stability in the operating voltage range of 3–8 V (Figures S37), indicating that efficient energy transfer and exciton recombination are stably confined within the EML.

3. Conclusion

In conclusion, we propose a strategy for azepination-induced FMO delocalization of MR emitters, that is, embedding azepine into the prototype molecule BNCz can effectively improve the π -conjugation degree and extend the FMO delocalization, thereby constructing a series of long-wavelength MR-TADF materials with narrowband emission: *m*-PAz-BNCz, *m*-SFAz-BNCz, *m*-DPAcPAz-BNCz and *m*-TPAz-BNCz. They all exhibit efficient green emission around 520 nm and narrow FWHMs of ≤ 38 nm in toluene solution. OLEDs employing these four emitters show excellent EL performances, among which *m*-PAz-BNCz-based OLED exhibits the optimal EL performances with a peak of 528 nm, a FWHM of 37 nm, CIE coordinates of (0.26, 0.70), and a maximum EQE of 36.2%. In fact, molecules *m*-SFAz-BNCz, *m*-DPAcPAz-BNCz and *m*-TPAz-BNCz can be regarded as further chemical modifications based on molecule *m*-PAz-BNCz. Since there are four substitutable sites on the peripheral benzene ring that encapsulates azepine, the modular synthetic route can be applied to the evolvable modification of model molecule *m*-PAz-BNCz with multifarious functional groups, such as donors, acceptors, and moieties without obvious push–pull electron properties. This programmed synthetic roadmap may provide new alternative strategies for the post-functionalization and structural modification of star MR emitter BNCz. In addition, the heptagonal azepine in *m*-PAz-BNCz is a derivative fragment of negatively curved carbon, which contains important structural information and can in principle serve as a template or monomer unit for the construction of heteroatom-embedded carbon schwarzites and toroidal carbon nanotubes, and its programmed synthetic route is a promising bottom-up synthetic

approach for the synthesis of many intriguing, aesthetic and imaginative carbon structures, especially B,N-embedded negatively curved nanographene.

Supporting Information

Supporting Information is available from the author.

Acknowledgements

This work was supported by the National Natural Science Foundation of China (21935005), the National Key R&D Program of China (2020YFA0714601), Jihua Laboratory (X190321TF190) and Foshan Science and Technology Innovation Team Special project (1920001000128).

Conflict of Interest

The authors declare no conflict of interest.

References

- [1] a) C. W. Tang, S. A. VanSlyke, *Appl. Phys. Lett.* **1987**, *51*, 913; b) P. Pust, P. J. Schmidt, W. Schnick, *Nat. Mater.* **2015**, *14*, 454; c) X. Yang, L. Ding, *J. Semicond.* **2021**, *42*, 090201.
- [2] a) E. Peli, ITU-R Recommendation BT, 2020: *Parameter Values for Ultrahigh Definition Television Systems for Production and International Programme Exchange*, International Telecommunication Union, **2012**; b) S. Takasugi, H.-J. Shin, M.-K. Chang, S.-M. Ko, H.-J. Park, J.-P. Lee, H.-S. Kim, C.-H. Oh, *J. Soc. Inf. Disp.* **2016**, *24*, 410; c) D. Wyatt, H. Chen, S.-T. Wu, *Soc. Inf. Disp. Int. Symp. Dig. Tech. Pap.* **2017**, *48*, 992.
- [3] a) H. Uoyama, K. Goushi, K. Shizu, H. Nomura, C. Adachi, *Nature*, **2012**, *492*, 234; b) T. Hatakeyama, K. Shiren, K. Nakajima, S. Nomura, S. Nakatsuka, K. Kinoshita, J. Ni, Y. Ono, T. Ikuta, *Adv. Mater.* **2016**, *28*, 2777; c) Y. Kondo, K. Yoshiura, S. Kitera, H. Nishi, S. Oda, H. Gotoh, Y. Sasada, M. Yanai, T. Hatakeyama, *Nat. Photonics* **2019**, *13*, 678.
- [4] a) A. Pershin, D. Hall, V. Lemaire, J.-C. Sancho-Garcia, L. Muccioli, E. Zysman-Colman, D. Beljonne, Y. Olivier, *Nat. Commun.* **2019**, *10*, 597; b) S. Wu, W. Li, K. Yoshida, D. Hall, S. M. Suresh, T. Sayner, J. Gong, D. Beljonne, Y. Olivier, I. D. W. Samuel, E. Zysman-Colman, *ACS Appl. Mater. Interfaces* **2022**, *14*, 22341; c) M. Mamada, M. Hayakawa, J. Ochi, T. Hatakeyama, *Chem. Soc. Rev.* **2023**, *53*, 1624.
- [5] a) S. M. Suresh, E. Duda, D. Hall, Z. Yao, S. Bagnich, A. M. Z. Slawin, H. Bässler, D. Beljonne, M. Buck, Y. Olivier, A. Köhler, E. Zysman-Colman, *J. Am. Chem. Soc.* **2020**,

- 142, 6588; b) S. Oda, B. Kawakami, Y. Yamasaki, R. Matsumoto, M. Yoshioka, D. Fukushima, S. Nakatsuka, T. Hatakeyama, *J. Am. Chem. Soc.* **2022**, *144*, 106; c) X. Wu, J.-W. Huang, B.-K. Su, S. Wang, L. Yuan, W.-Q. Zheng, H. Zhang, Y.-X. Zheng, W. Zhu, P.-T. Chou, *Adv. Mater.* **2022**, *34*, 2105080; d) J. Bian, S. Chen, L. Qiu, R. Tian, Y. Man, Y. Wang, S. Chen, J. Zhang, C. Duan, C. Han, H. Xu, *Adv. Mater.* **2022**, *34*, 2110547; e) H. J. Kim, T. Yasuda, *Adv. Opt. Mater.* **2022**, *10*, 2201714; f) F. Liu, Z. Cheng, Y. Jiang, L. Gao, H. Liu, H. Liu, Z. Feng, P. Lu, W. Yang, *Angew. Chem. Int. Ed.* **2022**, *61*, e202116927; g) Y. Liu, X. Xiao, Z. Huang, D. Yang, D. Ma, J. Liu, B. Lei, Z. Bin, J. You, *Angew. Chem. Int. Ed.* **2022**, *61*, e202210210; h) X. C. Fan, F. Huang, H. Wu, H. Wang, Y.-C. Cheng, J. Yu, K. Wang, X.-H. Zhang, *Angew. Chem. Int. Ed.* **2023**, *62*, e202305580; i) Y. X. Hu, J. Miao, T. Hua, Z. Huang, Y. Qi, Y. Zou, Y. Qiu, H. Xia, H. Liu, X. Cao, C. Yang, *Nat. Photonics* **2022**, *16*, 803; j) X.-C. Fan, K. Wang, Y.-Z. Shi, Y.-C. Cheng, Y.-T. Lee, J. Yu, X.-K. Chen, C. Adachi, X.-H. Zhang, *Nat. Photonics* **2023**, *17*, 280.
- [6] a) X. Liang, Z.-P. Yan, H.-B. Han, Z.-G. Wu, Y.-X. Zheng, H. Meng, J.-L. Zuo, W. Huang, *Angew. Chem. Int. Ed.* **2018**, *57*, 11316; b) J. Park, K. J. Kim, J. Lim, T. Kim, J. Y. Lee, *Adv. Mater.* **2022**, *34*, 2108581; c) H.-J. Cheon, S.-J. Woo, S.-H. Baek, J.-H. Lee, Y.-H. Kim, *Adv. Mater.* **2022**, *34*, 2207416; d) I. S. Park, M. Yang, H. Shibata, N. Amanokura, T. Yasuda, *Adv. Mater.* **2022**, *34*, 2107951.
- [7] a) Y. Zhang, D. Zhang, J. Wei, Z. Liu, Y. Lu, L. Duan, *Angew. Chem. Int. Ed.* **2019**, *58*, 16912; b) Y. Xu, Z. Cheng, Z. Li, B. Liang, J. Wang, J. Wei, Z. Zhang, Y. Wang, *Adv. Opt. Mater.* **2020**, *8*, 1902142; c) M. Yang, I. S. Park, T. Yasuda, *J. Am. Chem. Soc.* **2020**, *142*, 19468.
- [8] a) Y. Zhang, D. Zhang, J. Wei, X. Hong, Y. Lu, D. Hu, G. Li, Z. Liu, Y. Chen, L. Duan, *Angew. Chem. Int. Ed.* **2020**, *59*, 17499; b) Y. Qi, W. Ning, Y. Zou, X. Cao, S. Gong, C. Yang, *Adv. Funct. Mater.* **2021**, *31*, 2102017; c) J. Liu, Y. Zhu, T. Tsuboi, C. Deng, W. Lou, D. Wang, T. Liu, Q. Zhang, *Nat. Commun.* **2022**, *13*, 4876; d) X.-F. Luo, S.-Q. Song, H.-X. Ni, H. Ma, D. Yang, D. Ma, Y.-X. Zheng, J.-L. Zuo, *Angew. Chem. Int. Ed.* **2022**, *61*, e202209984; e) Y. Xu, Q. Wang, J. Wei, X. Peng, J. Xue, Z. Wang, S.-J. Su, Y. Wang, *Angew. Chem. Int. Ed.* **2022**, *61*, e202204652; f) Y. Zhang, D. Zhang, T. Huang, A. J. Gillett, Y. Liu, D. Hu, L. Cui, Z. Bin, G. Li, J. Wei, L. Duan, *Angew. Chem. Int. Ed.* **2021**, *60*, 20498.

- [9] a) Y. Xu, C. Li, Z. Li, Q. Wang, X. Cai, J. Wei, Y. Wang, *Angew. Chem. Int. Ed.* **2020**, *59*, 17442; b) Y. Xu, Q. Wang, X. Cai, C. Li, S. Jiang, Y. Wang, *Angew. Chem. Int. Ed.* **2023**, *62*, e202312451.
- [10] a) Y. Xu, C. Li, Z. Li, J. Wang, J. Xue, Q. Wang, X. Cai, Y. Wang, *CCS Chem.* **2022**, *4*, 2065; b) Q. Wang, Y. Xu, T. Yang, J. Xue, Y. Wang, *Adv. Mater.* **2023**, *35*, 2205166.
- [11] a) P. Jiang, J. Miao, X. Cao, H. Xia, K. Pan, T. Hua, X. Lv, Z. Huang, Y. Zou, C. Yang, *Adv. Mater.* **2022**, *34*, 2106954; b) J. Wang, N. Li, C. Zhong, J. Miao, Z. Huang, M. Yu, Y. X. Hu, S. Luo, Y. Zou, K. Li, C. Yang, *Adv. Mater.* **2023**, *35*, 2208378; c) Y. Zhang, J. Wei, D. Zhang, C. Yin, G. Li, Z. Liu, X. Jia, J. Qiao, L. Duan, *Angew. Chem. Int. Ed.* **2022**, *61*, e202113206; d) Y.-K. Qu, D.-Y. Zhou, F.-C. Kong, Q. Zheng, X. Tang, Y.-H. Zhu, C.-C. Huang, Z.-Q. Feng, J. Fan, C. Adachi, L.-S. Liao, Z.-Q. Jiang, *Angew. Chem. Int. Ed.* **2022**, *61*, e202201886; e) T. Wang, Y. Zou, Z. Huang, N. Li, J. Miao, C. Yang, *Angew. Chem. Int. Ed.* **2022**, *61*, e202211172; f) S. Cai, G. S. M. Tong, L. Du, G. K.-M. So, F.-F. Hung, T.-L. Lam, G. Cheng, H. Xiao, X. Chang, Z.-X. Xu, C.-M. Che, *Angew. Chem. Int. Ed.* **2022**, *61*, e202213392; g) Y. Hu, J. Miao, C. Zhong, Y. Zeng, S. Gong, X. Cao, X. Zhou, Y. Gu, C. Yang, *Angew. Chem. Int. Ed.* **2023**, *62*, e202302478; h) T. Wang, X. Yin, X. Cao, C. Yang, *Angew. Chem. Int. Ed.* **2023**, *62*, e202301988; i) G. Chen, J. Wang, W.-C. Chen, Y. Gong, N. Zhuang, H. Liang, L. Xing, Y. Liu, S. Ji, H.-L. Zhang, Z. Zhao, Y. Huo, B. Z. Tang, *Adv. Funct. Mater.* **2023**, *33*, 2211893; j) F. Huang, X.-C. Fan, Y.-C. Cheng, Y. Xie, S. Luo, T. Zhang, H. Wu, X. Xiong, J. Yu, D.-D. Zhang, X.-K. Chen, K. Wang, X.-H. Zhang, *Adv. Opt. Mater.* **2023**, *11*, 2202950; k) F. Huang, Y.-C. Cheng, H. Wu, X. Xiong, J. Yu, X.-C. Fan, K. Wang, X.-H. Zhang, *Chem. Eng. J.* **2023**, *465*, 142900.
- [12] a) M.-Y. Chen, F. Huang, H. Wu, Y.-C. Cheng, H. Wang, Y.-N. Hu, X.-C. Fan, J. Yu, K. Wang, X.-H. Zhang, *Mater. Horiz.* **2023**, *10*, 4224; b) S.-Q. Song, C.-F. Yip, Q.-M. Liu, X.-S. Zhong, Y. Wang, Y.-X. Zheng, *Adv. Opt. Mater.* **2024**, 2400200.
- [13] S. H. Pun, Q. Miao, *Acc. Chem. Res.* **2018**, *51*, 1630.
- [14] a) S. Grimme, S.D. Peyerimhoff, *Chem. Phys.* **1996**, *204*, 411; b) P. Ravat, R. Hinkelmann, D. Steinebrunner, A. Prescimone, I. Bodoky, M. Juricek, *Org. Lett.* **2017**, *19*, 3707.
- [15] R. M. Soneira, *Inf. Disp.* **2016**, *32*, 26.
- [16] a) D. P. McMahon, A. Troisi, *J. Phys. Chem. Lett.* **2010**, *1*, 941; b) Z. Pei, Q. Ou, Y. Mao, J. Yang, A. d. I. Lande, F. Plasser, W. Liang, Z. Shuai, Y. Shao, *J. Phys. Chem. Lett.* **2021**, *12*, 2712.

- [17] a) T. J. Zuehlsdorff, C. M. Isborn, *J. Chem. Phys.* **2018**, *148*, 024110; b) H. Mustroph, *ChemPhysChem* **2016**, *17*, 2616; c) X. Qiu, G. Tian, C. Lin, Y. Pan, X. Ye, B. Wang, D. Ma, D. Hu, Y. Luo, Y. Ma, *Adv. Opt. Mater.* **2021**, *9*, 2001845.
- [18] G. Bolla, Q. Liao, S. Amirjalayer, Z. Tu, S. Lv, J. Liu, S. Zhang, Y. Zhen, Y. Yi, X. Liu, H. Fu, H. Fuchs, H. Dong, Z. Wang, W. Hu, *Angew. Chem., Int. Ed.* **2021**, *60*, 281.
- [19] Z. Liu, T. Lu, Q. Chen, *Carbon* **2020**, *165*, 468.
- [20] M. S. Abdollahi, E. Nemati-Kande, A. P. Marjani, *ChemistrySelect* **2020**, *5*, 3971.
- [21] Q. Wang, L. Yuan, C. Qu, T. Huang, X. Song, Y. Xu, Y.-X. Zheng, Y. Wang, *Adv. Mater.* **2023**, *35*, 2305125.
- [22] C. Murawski, K. Leo, M. C. Gather, *Adv. Mater.* **2013**, *25*, 6801.
- [23] a) H. Nakanotani, T. Higuchi, T. Furukawa, K. Masui, K. Morimoto, M. Numata, H. Tanaka, Y. Sagara, T. Yasuda, C. Adachi, *Nat. Commun.* **2014**, *5*, 4016; b) D. Zhang, X. Song, M. Cai, L. Duan, *Adv. Mater.* **2018**, *30*, 1705250.
- [24] H. Kaji, H. Suzuki, T. Fukushima, K. Shizu, K. Suzuki, S. Kubo, T. Komino, H. Oiwa, F. Suzuki, A. Wakamiya, Y. Murata, C. Adachi, *Nat. Commun.* **2015**, *6*, 8476.
- [25] a) S. S. Skourtis, C. Liu, P. Antoniou, A. M. Virshup, D. N. Beratan, *Proc. Natl. Acad. Sci. U. S. A.* **2016**, *113*, 8115; b) H. Mubarak, A. Amin, T. Lee, J. Jung, J.-H. Lee, M. H. Lee, *Angew. Chem., Int. Ed.* **2023**, *62*, e202306879.

Table of Contents

A strategy for azepination-induced frontier molecular orbital (FMO) delocalization of multiple resonance (MR) emitters has been proposed, that is, embedding azepine into the prototype molecule BNCz can effectively improve the π -conjugation degree and extend the FMO delocalization, thereby constructing long-wavelength MR materials. Organic light-emitting diode based on *m*-PAz-BNCz exhibits excellent electroluminescence performances with Commission Internationale de L'Eclairage coordinates of (0.26, 0.70) and a maximum external quantum efficiency of 36.2%.

